

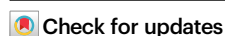


Photo-thermal coupling to enhance CO₂ hydrogenation toward CH₄ over Ru/MnO/Mn₃O₄

Received: 5 July 2023

Accepted: 19 January 2024

Published online: 06 February 2024

Jianxin Zhai^{1,2}, Zhanghui Xia^{1,2}, Baowen Zhou³✉, Haihong Wu^{1,2}✉, Teng Xue^{1,2}, Xiao Chen^{1,2}, Jiapeng Jiao^{1,2}, Shuaiqiang Jia^{1,2}, Mingyuan He^{1,2}✉ & Buxing Han^{1,2,4}✉

Upcycling of CO₂ into fuels by virtually unlimited solar energy provides an ultimate solution for addressing the substantial challenges of energy crisis and climate change. In this work, we report an efficient nanostructured Ru/MnO_x catalyst composed of well-defined Ru/MnO/Mn₃O₄ for photo-thermal catalytic CO₂ hydrogenation to CH₄, which is the result of a combination of external heating and irradiation. Remarkably, under relatively mild conditions of 200 °C, a considerable CH₄ production rate of 166.7 mmol g⁻¹ h⁻¹ was achieved with a superior selectivity of 99.5% at CO₂ conversion of 66.8%. The correlative spectroscopic and theoretical investigations suggest that the yield of CH₄ is enhanced by coordinating photon energy with thermal energy to reduce the activation energy of reaction and promote formation of key intermediate COOH* species over the catalyst. This work opens up a new strategy for CO₂ hydrogenation toward CH₄.

Upcycling of CO₂ into fuels with the use of green hydrogen presents a promising route for addressing the challenges of energy crisis and climate change^{1–3}. Among a variety of products from CO₂ hydrogenation, CH₄ is regarded as an ideal energy vector owing to its merits of high energy density, widely available infrastructure of storage, transportation, and utilization^{4,5}. To date, a broad range of catalytic systems have been developed for CO₂ hydrogenation toward CH₄⁶. However, because of the inert nature of CO₂ and complex reaction network, efficient production of CH₄ from CO₂ hydrogenation is challenging, suffering from unsatisfactory activity, harsh reaction condition and extensive thermal input^{7–9}. It is imperative to explore new and green methods for the conversion of CO₂ toward CH₄.

Photo-thermal-catalysis presents a synergistic configuration for mediating chemical reactions by simultaneously taking advantage of charge carriers and thermal energy^{10,11}. Thus far, there is a growing

number of researches on photo-thermal catalytic CO₂ hydrogenation toward CH₄ and remarkable progress has been made^{12,13}. For example, Liu et al. reported that Co₇Cu₁Mn₁O_x (200) was active for CH₄ synthesis from CO₂ hydrogenation with an production rate of 14.5 mmol g⁻¹ h⁻¹ and a selectivity of 85.3% at 200 °C¹⁴. Zou's group demonstrated that Ru@Ni₂V₂O₇ catalyst exhibited CH₄ production rate of 114.9 mmol g⁻¹ h⁻¹ and 99.3% selectivity at 350 °C¹⁵. Overall, the performance of the catalytic systems is still far away from practical applications and the reaction mechanism remains largely unknown¹⁶. It is very desirable to explore a strategy for mediating CO₂ hydrogenation toward CH₄ with high efficiency and selectivity¹⁷.

Among a broad range of CO₂ hydrogenation catalysts, Ru-based catalysts exhibit great potential in CO₂ hydrogenation toward CH₄ because of their unique catalytic properties¹⁸. Apart from metal centers, the support also plays a critical role in CO₂ hydrogenation by

¹Shanghai Key Laboratory of Green Chemistry and Chemical Processes, State Key Laboratory of Petroleum Molecular & Process Engineering, School of Chemistry and Molecular Engineering, East China Normal University, Shanghai 200062, China. ²Institute of Eco-Chongming, Shanghai 202162, China. ³Key Laboratory for Power Machinery and Engineering of Ministry of Education, Research Center for Renewable Synthetic Fuel, School of Mechanical Engineering, Shanghai Jiao Tong University, Shanghai 200240, China. ⁴Beijing National Laboratory for Molecular Sciences, CAS Key Laboratory of Colloid and Interface and Thermodynamics, CAS Research/Education Center for Excellence in Molecular Sciences, Institute of Chemistry, Chinese Academy of Sciences, Beijing 100190, China. ✉ e-mail: zhoubw@sjtu.edu.cn; hwwu@chem.ecnu.edu.cn; Mingyuanhe@126.com; hanbx@iccas.ac.cn

influencing the geometric and electronic properties of active sites. Particularly, MnO_x is considered a promising support for hydrogenation reactions due to some obvious advantages¹⁹. It is worth of noting that the multiple valences and reducible effect of MnO_x confers flexible mediation capability on the catalysts²⁰. The integration of Ru species with MnO_x is thus highly promising for efficient CO_2 hydrogenation toward CH_4 .

In this work, a nanostructured Ru/ MnO_x photo-thermal catalyst composed of well-defined Ru/ $\text{MnO}/\text{Mn}_3\text{O}_4$ at reaction temperature was designed and prepared for CO_2 hydrogenation toward CH_4 . A prominent CO_2 conversion of 66.8% was achieved with a superior selectivity of 99.5% and a CH_4 production rate of $166.7 \text{ mmol g}^{-1} \text{ h}^{-1}$ at relatively mild temperature of 200°C (normalized by the amount of catalyst ($\sim 15 \text{ mg}$)), which is the result of a combination of external heating and irradiation. The correlative spectroscopic characterizations and theoretical calculations revealed that the structural evolution of Ru/ MnO_x into well-defined Ru/ $\text{MnO}/\text{Mn}_3\text{O}_4$ was facilitated by Ru-mediated H-spillover in MnO_x and the activity was enhanced by the synergistic effects of photon energy and thermal energy via reducing the activation energy of reaction and accelerating the key intermediate of COOH^* species formation over the catalyst.

Results

Fabrication and characterization of Ru/ MnO_x

The synthesis process of Ru/ MnO_x was schematically shown in Fig. 1a. Typically, MnO_x nanoparticles were first prepared via a straightforward hydrothermal method. Ru sites were then anchored onto MnO_x by photo-deposition under argon atmosphere²¹. The content of Ru in

Ru/ MnO_x was measured by inductively coupled plasma optical emission spectrometry (ICP-OES) (Supplementary Table 1). If not specifically noted, the content of Ru in Ru/ MnO_x was referred to be 7.3 wt%. The morphologies and structures of the synthesized materials were characterized by scanning electron microscopy (SEM) and transmission electron microscopy (TEM). As shown in Figs. 1b, c, MnO_x displayed variable morphologies of hexagonal, octahedral, and square schistose crystals. The morphology of MnO_x did not change considerably after the addition of Ru species and the average size of the deposited Ru nanoclusters is about $1.07 \pm 0.26 \text{ nm}$ (Fig. 1d and Supplementary Figs. 1, 2). The energy dispersive spectroscopy elemental mapping in Fig. 1e exhibited the even distribution of Mn, O, and Ru, which is indicative of the successful synthesis of Ru/ MnO_x .

The Rietveld refinement of X-ray powder diffraction (XRD) results in Supplementary Fig. 3 and Supplementary Table 2 indicated that the MnO_x nanoparticles were mainly composed of Mn_3O_4 (JCPDS No. 80-0382), MnO_2 (JCPDS 72-1806) and MnOOH (JCPDS No. 18-0804)²²⁻²⁴. Meanwhile, the XRD pattern of Ru/ MnO_x showed that the content of MnO_2 phase decreased slightly, indicating that the process of photo-deposition of Ru had a slight reduction effect on MnO_2 . The structure of the samples was further characterized by Fourier transform infrared spectroscopy (FT-IR) spectroscopy (Supplementary Fig. 4). The peaks at 513 and 621 cm^{-1} were attributed to the distortion vibration of Mn-O in octahedral sites and Mn-O stretching modes in tetrahedral sites, respectively²⁵. Besides, the typical peaks at 947 and 1074 cm^{-1} were attributed to the vibration of hydroxyl in MnOOH ²⁶. Meanwhile, Raman spectrometer was employed to study the metal-support interaction between Ru and MnO_x . As illustrated in Supplementary Fig. 5,

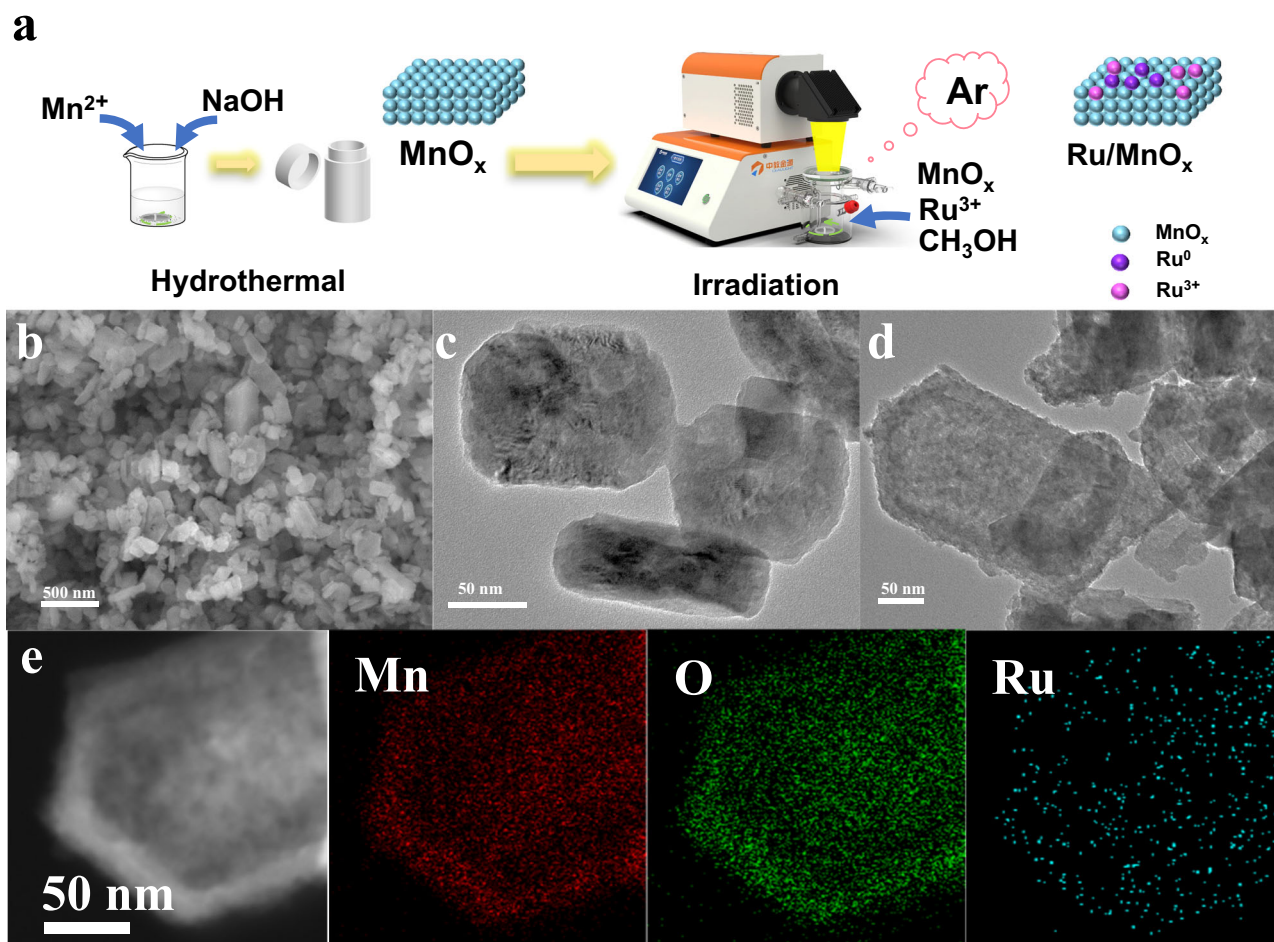


Fig. 1 | Structural characterization of the catalysts. **a** Schematic illustration of the synthesis of Ru/ MnO_x ; **b** SEM image of MnO_x ; **c**, **d** TEM image of MnO_x and Ru/ MnO_x ; **e** STEM image and elemental mapping of Ru/ MnO_x .

compared with the pristine MnO_x , the introduction of Ru species led to a blue shift of ~ 7 wavenumbers, and the main peak at 637 cm^{-1} is assigned to A_{1g} mode of crystalline Mn_3O_4 , validating the strong metal–support interaction between Ru and MnO_x ²⁷. Moreover, as characterized by CO_2 adsorption isotherm and N_2 adsorption–desorption isotherms, the addition of Ru species enhanced the CO_2 adsorption capacity; and specific surface area of the catalyst was enlarged accordingly (Supplementary Figs. 6, 7). Such improvements are beneficial for the interaction between reactants and mass transfer, thus facilitating CO_2 methanation. In addition, X-ray photoelectron spectroscopy (XPS) was examined to gain more insight into surface chemical state and electronic structure of the catalysts (Supplementary Fig. 8). For Ru/ MnO_x , Ru^0 is identified by the peaks observed at ca. 462.7 and 484.8 eV, implying the reduction of Ru species under light irradiation²⁸. Additionally, XPS analysis of the Mn species in all tested samples can be deconvoluted into Mn^{4+} , Mn^{3+} , and Mn^{2+} ^{23,27}. Apparently, multiple valences of MnO_x indicate the reducible nature of as-prepared catalyst.

Photo-thermal catalytic CO_2 hydrogenation

The catalytic performance of Ru/ MnO_x was evaluated at $200\text{ }^\circ\text{C}$ in the batch reactor setup by feeding CO_2/H_2 mixed gas (the desired temperature was achieved by a combination of external heating and irradiation from the Xe lamp) and CH_4 was identified as the dominant product, with no liquid products produced (Supplementary Figs. 9, 10). As shown in Fig. 2a, MnO_x was hardly active for CO_2 hydrogenation toward CH_4 . In contrast, after the addition of Ru species into MnO_x , considerable activity for CH_4 formation was achieved, indicating that Ru species could serve as effective active site for the reaction. Notably, the catalytic activity of Ru/ MnO_x gradually increased with an increasing amount of Ru. At a Ru content of 7.3 wt%, the catalyst displayed a decent CH_4 activity of $103.7\text{ mmol g}^{-1}\text{ h}^{-1}$. The CH_4 activity was increased by further increasing the loading content of Ru, but the trend slowed down. The effect of CO_2/H_2 ratios on the yield of CH_4 was then examined. It was observed that the yield of CH_4 monotonically

increased with the H_2 proportion in the H_2/CO_2 mixture (Fig. 2b). A distinct CH_4 production rate of $166.7\text{ mmol g}^{-1}\text{ h}^{-1}$ was obtained for Ru/ MnO_x at a relatively high H_2/CO_2 ratio of 4/1, highlighting the importance of adequate H_2 supply during the reaction to enhance its activity. Furthermore, as shown in Supplementary Fig. 11, we studied the influence of the total pressure on the reaction at high H_2/CO_2 ratio (4/1). The activity was enhanced markedly with the elevating total pressure, but became slowly when the pressure exceeded 1 MPa.

As shown in Supplementary Fig. 12, the control experiment showed that no carbonaceous products were detected without catalyst or reactant gas, confirming that CH_4 was catalytically produced from CO_2 hydrogenation. Furthermore, when the photon energy was coupled with external thermal energy, the evolution rate of CH_4 was substantially enhanced compared to that achieved by thermo-catalysis in the temperature range examined (Fig. 2c). In addition, when the reaction temperature was kept at $200\text{ }^\circ\text{C}$ by an external temperature-controlling system, the CH_4 evolution rate of Ru/ MnO_x could be further enhanced by increasing the light intensity, reaching $166.7\text{ mmol g}^{-1}\text{ h}^{-1}$ at 2.5 W cm^{-2} (Fig. 2d). These results provide solid support that the introduction of photon energy can significantly enhance CO_2 hydrogenation reaction. Meanwhile, the activation energies of Ru/ MnO_x under thermal and photo-thermal conditions were estimated to be 99.9 and 68.5 kJ mol^{-1} , respectively (Fig. 2e). The decreased activation energy and the corresponding non-parallel plots were indicative of a synergy between photon energy and thermal energy, altering the catalytic mechanism when photons were involved. Moreover, the conversion of CO_2 toward CH_4 as a function of reaction time is shown in Fig. 2f. It was found that the yield of CH_4 continuously increased with the reaction time, suggesting the continuous generation of CH_4 from CO_2 hydrogenation over Ru/ MnO_x . Impressively, with a reaction time of 4 h at $200\text{ }^\circ\text{C}$, a considerable CO_2 conversion of 66.8% was achieved with a high selectivity of 99.5% with an appreciable CH_4 production rate of $166.7\text{ mmol g}^{-1}\text{ h}^{-1}$. Furthermore, the photo-thermal catalytic performance of the Ru/ MnO_x catalyst was also assessed in a fixed-bed reactor. As shown in Supplementary Figs. 13, 14,

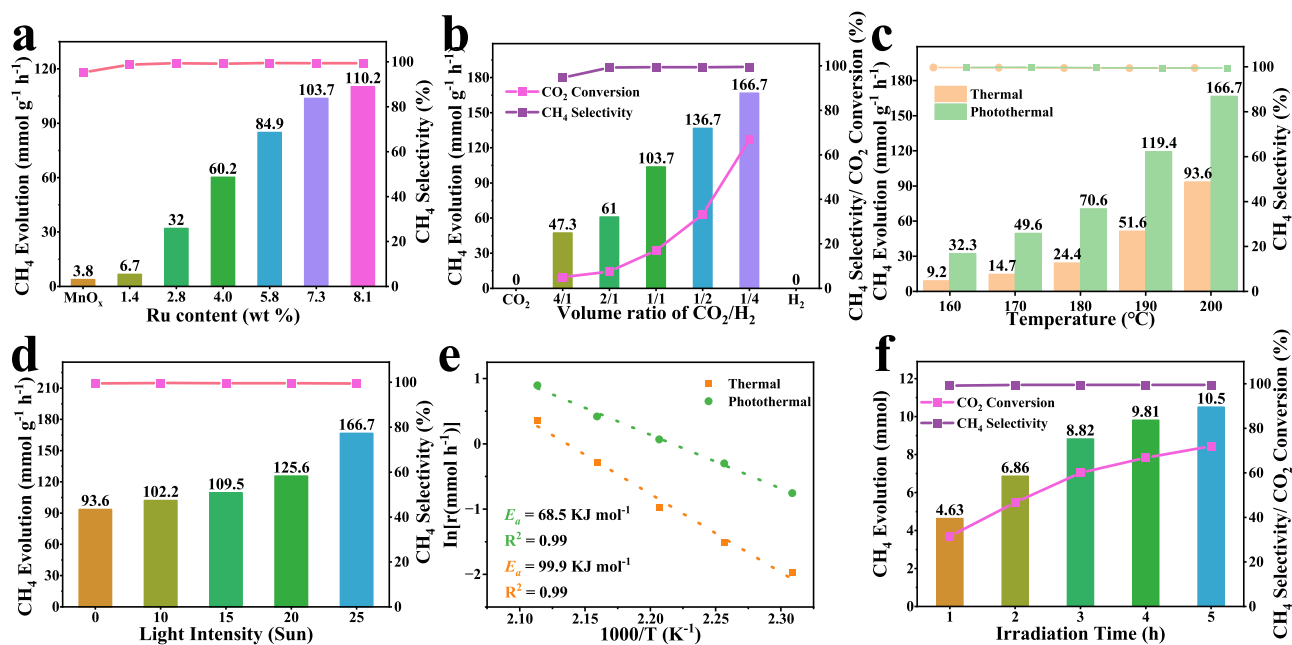


Fig. 2 | Photo-thermal-catalytic performance. **a** Influence of the Ru content on CH_4 evolution rate over Ru/ MnO_x ; **b** Influence of CO_2/H_2 volume ratio in the feedstock on CH_4 evolution rate over Ru/ MnO_x ; **c** Temperature-dependent CH_4 generation rate over Ru/ MnO_x under photo-thermal and thermal conditions; **d** Influence of light intensity on CH_4 evolution rate over Ru/ MnO_x ; **e** Corresponding

Arrhenius plot with activation energies noted under photo-thermal/thermal conditions over the Ru/ MnO_x catalysts. **f** CH_4 evolution as a function of reaction time over Ru/ MnO_x . Reaction conditions: 15 mg of catalyst, full-arc 300 W UV-xenon lamp, 2.5 W cm^{-2} , $200\text{ }^\circ\text{C}$, irradiation time 4 h, initial pressure 1 MPa ($\text{H}_2/\text{CO}_2 = 1/1$) for Fig. 2a or initial pressure 1 MPa ($\text{H}_2/\text{CO}_2 = 4/1$) for Fig. 2c–f.

at a gas hourly space velocity (GHSV) of $20,000 \text{ mL g}^{-1} \text{ h}^{-1}$, the catalytic activity of Ru/MnO_x gradually increased with an increasing temperature, and its activities under photothermal conditions were higher than those under thermal conditions, which further proves that the involved photons were prone to promote the formation of CH_4 in the fixed-bed reactor. Meanwhile, under the conditions of 200°C and 2.5 W cm^{-2} irradiation, the catalytic activity of Ru/MnO_x remained acceptably stable after 20 h at a high GHSV of $40,000 \text{ mL g}^{-1} \text{ h}^{-1}$ (Supplementary Fig. 15). A CO_2 conversion of 29.5% was achieved with an excellent selectivity of 99.5% and a high space-time yield (STY) of $95.8 \text{ mmol}_{\text{CH}_4} \text{ g}^{-1} \text{ h}^{-1}$. The decrease in activity was probably caused by catalyst agglomeration and carbon deposition as confirmed by the TEM and Thermogravimetric-mass spectrometric (TG-MS) of the catalyst after the reaction (Supplementary Figs. 16, 17). In addition, as characterized by XPS, for Ru/MnO_x , after the reaction, the composition of Mn^{4+} disappeared, and the peak appearing at 647 eV is the satellite peak of Mn^{2+} , demonstrating that the multiphase MnO_x support underwent partial reduction²⁹. Ru species were completely converted into Ru^0 , indicating that the in-situ generated Ru can act as a metal active center to enhance the dissociation of H_2 and spillover of hydrogen to the MnO_x support (Supplementary Fig. 18). Therefore, the actual composition of the catalyst during the reaction was altered, and the observations above suggested the H-spillover effects in Ru/MnO_x , which will be discussed further in the following.

Origin of the superior activity over Ru/MnO_x

The optical and electronic properties of the catalyst play a vital role in photo-thermal-catalytic activity. Thereby, they were characterized by various spectroscopy techniques. Firstly, the UV-Vis-NIR diffuse reflectance spectra of different samples were measured to study the light absorption capacity. As illustrated in Fig. 3a, MnO_x , as an excellent semiconducting support, exhibits suitable light absorption in the UV-Vis region. The light absorption of MnO_x was further improved by the addition of Ru species, having stronger and broader light absorption from UV to NIR wavelength. Meanwhile, due to the broadening of the wavelength range of light absorption, a strong photothermal effect was expected^{30,31}. As shown in Supplementary Fig. 19, under 2.5 W cm^{-2} illumination, the measured average temperature of Ru/MnO_x reached 137.9°C , higher than that of MnO_x (115.4°C), indicating that both Ru and MnO_x contributed to the photothermal effect. In addition, time-resolved photoluminescence spectroscopy showed that the charge carriers lifetime of bare MnO_x ($\tau_1 = 1.05 \text{ ns}$, $\tau_2 = 13.51 \text{ ns}$) was obviously prolonged by the incorporation of Ru species ($\tau_1 = 1.33 \text{ ns}$, $\tau_2 = 17.14 \text{ ns}$ for Ru/MnO_x) in Supplementary Fig. 20³². The behavior of charge carriers was further investigated by transient photocurrent spectra, and the results are plotted in Supplementary Fig. 21. Under light irradiation, Ru/MnO_x exhibits a significantly higher photocurrent intensity than MnO_x ³³. The results above show that both optical and electronic properties of MnO_x were enhanced by the introduction of Ru species.

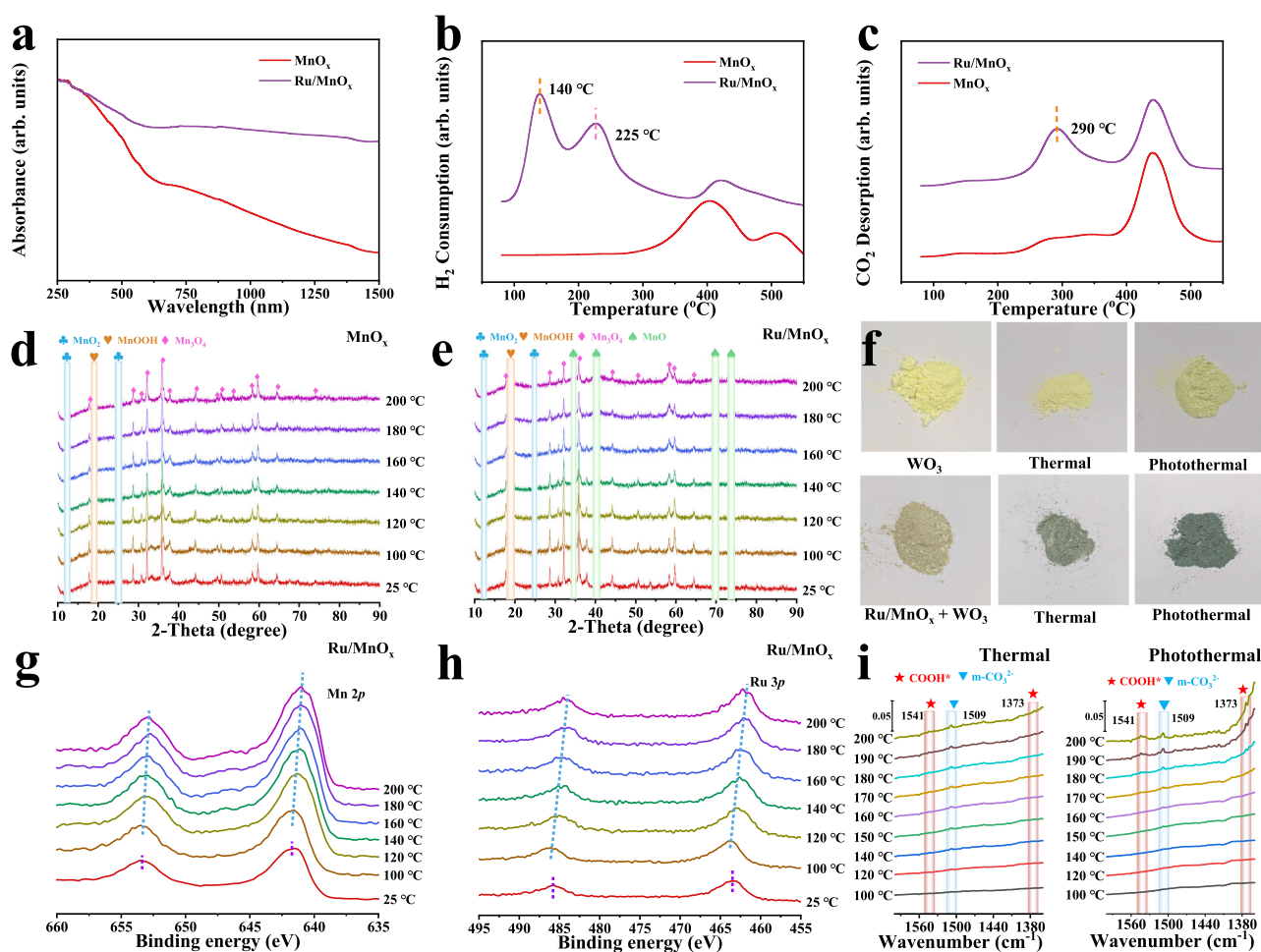


Fig. 3 | The mechanism analysis. **a** UV-Vis-IR absorption spectra of MnO_x and Ru/MnO_x ; **b** H_2 -TPR and **c** CO_2 -TPD characterization for MnO_x and Ru/MnO_x ; **d**, **e** The variable-temperature XRD patterns of MnO_x and Ru/MnO_x recorded under 20% CO_2/H_2 atmosphere at different temperatures; **f** Photographs of WO_3 and the

mixture of Ru/MnO_x and WO_3 samples after treatment with H_2 at 80°C with a light intensity of 0.3 W cm^{-2} for 20 min; **g**, **h** XPS spectra of Ru/MnO_x in 20% CO_2/H_2 atmosphere under variable temperature; **i** Spectra of FT-IR study of Ru/MnO_x at different conditions.

Moreover, the flat band potentials of MnO_x were investigated by Mott-Schottky plots. As shown in Supplementary Fig. 22a, MnO_x is confirmed as a p-type semiconductor due to the negative slope. Meanwhile the valence band edge potential was evaluated to be c.a. 0.29 (0.49 eV vs. NHE, $E_{\text{NHE}} = E_{\text{Ag/AgCl}} + 0.197$), while the flat-band potential is 0.1–0.3 eV lower than the valence band potential in the p-type semiconductor³⁴. In addition, the band gap can be estimated to be 1.26 eV for MnO_x (Supplementary Fig. 22b). Consequently, as shown in Supplementary Fig. 23, considering that the work function of Ru is 4.71 eV, the photo-excited electrons can facilitate transfer from MnO_x to Ru sites under light irradiation³⁵. Together with the unique catalytic properties, the assembled photo-thermal catalyst of Ru/ MnO_x was therefore highly efficient and selective for catalyzing CO_2 hydrogenation toward CH_4 .

The characterizations of H_2 temperature programmed reduction (H_2 -TPR) and CO_2 temperature programmed desorption (CO_2 -TPD) were performed to figure out the important role of Ru and MnO_x in CO_2 methanation. Compared to pristine MnO_x , Ru/ MnO_x exhibited remarkably lowered H_2 reduction temperature, which was as low as 140 °C (Fig. 3b), suggesting the superior H_2 activation capacity of Ru species. The temperature of H_2 activation over Ru/ MnO_x was even much lower than that for CO_2 hydrogenation (200 °C). Hence, CO_2 hydrogenation could benefit from low-temperature H_2 activation by Ru species under experimental conditions. Moreover, upon the introduction of Ru species, the reduction temperature peaks of MnO_x were observed to emerge at low temperature range of 180–250 °C. Herein, the partial reduction of the support MnO_x was probably associated with the hydrogen dissociation on Ru and its subsequent spillover to MnO_x ³⁶. The CO_2 adsorption properties were then evaluated by CO_2 -TPD. As shown in Fig. 3c, compared to pristine MnO_x , Ru/ MnO_x showed remarkable desorption peaks between 250 and 350 °C, indicating that Ru species obviously enhanced the adsorption of CO_2 ³⁷. Therefore, the dissociated H can further modulate the hydrogenation activity by directly reacting with CO_2 adsorbed on Ru sites or MnO_x support, thereby exerting a positive impact on the methanation.

To further explore the Ru-mediated H-spillover effect on the structural composition of Ru/ MnO_x , qualitative analysis of the crystal phases of Ru/ MnO_x during the CO_2 methanation process was conducted by variable temperature XRD measurements, with a focus on revealing the structural evolution of MnO_x at different stages. As illustrated in Fig. 3d, e, all the tested samples are primarily composed of Mn_3O_4 , MnO_2 , and MnOOH . For MnO_x , MnO_2 phase can be reduced when the temperature reaches 100 °C. Meanwhile, the transformation of MnOOH to Mn_3O_4 phase is observed between 100 and 200 °C. In contrast, the Mn_3O_4 phase remains stable at least 4 h at 200 °C (Supplementary Fig. 24). Interestingly, upon the introduction of Ru species, the variable temperature XRD patterns of Ru/ MnO_x showed notable changes. The terminal transforming temperature of MnOOH phase markedly decreases from 200 °C to 140 °C. Then, MnO (JCPDS No. 80-0382) with diffraction peaks at 34.7° (111), 40.5° (200), 70.1° (311) and 73.8° (222) were formed when the temperature rises from 140 °C to 200 °C. The observation above is well consistent with the H_2 -TPR characterization³⁸. As a result, the assembled photo-thermal catalyst of Ru/ MnO_x was composed of MnO phase and Mn_3O_4 phase at 200 °C. The phases of materials could remain stable at least 4 h at 200 °C, implying that the Ru/ MnO_x photo-thermal catalyst composed of well-defined Ru/ $\text{MnO}/\text{Mn}_3\text{O}_4$ can efficiently and stably catalyze CO_2 hydrogenation to CH_4 at reaction temperature. Therefore, the phase transformation of multiple-phase MnO_x is clearly indicative of Ru-mediated H-spillover effect. Furthermore, as shown in Supplementary Fig. 25, the catalytic activity of MnO_x supports surpasses that of the other specific manganese oxide alone. It indicates that the H-spillover effect in Ru/ MnO_x can effectively transfer dissociated H to the support

due to the multivalent states ($\text{Mn}^{2+}/\text{Mn}^{3+}/\text{Mn}^{4+}$) with varied reducibility, thereby promoting the hydrogenation reaction.

In addition, to investigate the impact of photons on the H-spillover effect under photothermal conditions, we employed WO_3 as a means to quantify the extent of H-spillover effect, by which the spillover hydrogen can migrate and readily react with yellow WO_3 , resulting in a dark coloration^{39,40}. The experiment was conducted at 80 °C with a light intensity of 0.3 W cm^{-2} under 1 MPa H_2 to ensure that the temperature induced by the photothermal effect remained below the designated temperature (Supplementary Fig. 26). As shown in Fig. 3f, it was revealed that the color of WO_3 remained unchanged under both photothermal and thermal conditions. In contrast, the mixture of Ru/ MnO_x and WO_3 exhibited a darker color under photothermal conditions compared to thermal conditions. This observation suggests that under photothermal catalysis, the irradiation can enhance the H-spillover effect, thereby promoting the subsequent CO_2 hydrogenation reaction.

Meanwhile, XPS was performed to gain insight into the composition and chemical valence. As can be observed in Fig. 3g, h and Supplementary Fig. 27, Ru 3p and Mn 2p peaks of Ru/ MnO_x displayed a negative shift from 100 °C to 200 °C. Then, the Mn 2p and Ru 3p spectra remain unvaried within 4 h at 200 °C, which is in good agreement with the variable XRD measurements. Supplementary Fig. 28 shows that the binding energies of Ru shift to 462.7 eV, corresponding to Ru^0 and the peaks of Mn^{4+} disappeared. The peak at 647 eV is the satellite peak of Mn^{2+} . Such binding energy shifts indicate that Ru^{3+} and Mn^{4+} were reduced under the CO_2/H_2 mixed gas ($\text{H}_2:\text{CO}_2 = 4:1$), which is consistent with the H_2 -TPR characterization.

To better understand the reaction at molecular level and explore the impact of the involved photon on the reaction, CO_2 hydrogenation was studied by FT-IR under different conditions (Fig. 3i and Supplementary Figs. 29, 30). For thermocatalysis, the typical peaks of monodentate carbonates (m-CO_3^{2-} , 1509 cm^{-1}) and $\nu(\text{C-H})$ vibration of CH_4 (1305 cm^{-1}) were apparently strengthened by increasing the reaction temperature^{41,42}. Notably, the intermediate of formate species was observed at 1541 cm^{-1} (COOH^* , $\nu(\text{OCO})_{\text{as}}$) and 1373 cm^{-1} (COOH^* , $\nu(\text{OCO})_{\text{s}}$) when the reaction temperature increased up to 200 °C⁴³. In contrast, upon light irradiation, the typical peaks of COOH^* species appeared at a lower reaction temperature of 170 °C⁴⁴. This finding further validated the synergy between photon energy and thermal energy on CO_2 hydrogenation toward CH_4 , and COOH^* is the most likely key intermediate during either thermo-catalysis or photo-thermal-catalysis. Hence, the involved photons were prone to accelerate the formation of intermediate species, thus can significantly reduce the activation energy of CO_2 hydrogenation reaction and promote the formation of CH_4 .

To better understand the mechanism of the superior performance, first-principles density functional theory calculations were carried out on the basis of the models of Ru/ Mn_3O_4 (321) slabs, Ru/ MnO (200) slabs and Ru/ $\text{Mn}_3\text{O}_{4-x}$ (321) slabs that simulated the partial reduction of Mn_3O_4 by the H-spillover effect (Supplementary Fig. 31)⁴⁵. As shown in Fig. 4 and Supplementary Fig. 32–34, Ru/ $\text{Mn}_3\text{O}_{4-x}$ has a more negative Gibbs free energy (ΔG) than both Ru/ Mn_3O_4 and Ru/ MnO during the adsorption of CO_2 , indicating a strong adsorption capacity for CO_2 , which is beneficial for CO_2 hydrogenation ($\Delta G = -0.914$ eV, Ru/ MnO ; $\Delta G = -1.475$ eV, Ru/ Mn_3O_4 ; $\Delta G = -1.651$ eV, Ru/ $\text{Mn}_3\text{O}_{4-x}$). Afterwards, notable variations for the subsequent CO_2 hydrogenation were observed among Ru/ MnO , Ru/ Mn_3O_4 , and Ru/ $\text{Mn}_3\text{O}_{4-x}$. The formation of COOH^* from CO_2^* is a rate determining step (RDS) for CO_2 hydrogenation over Ru/ $\text{Mn}_3\text{O}_{4-x}$ and Ru/ MnO , which requires 1.232 and 1.544 eV, respectively. The protonation and subsequent dehydration of COOH^* results in the generation of the intermediate of CO^* , which is the RDS for the Ru/ Mn_3O_4 ($\Delta G = 1.918$ eV for Ru/ Mn_3O_4). Notably, compared to HCO^* formation, the CO^*

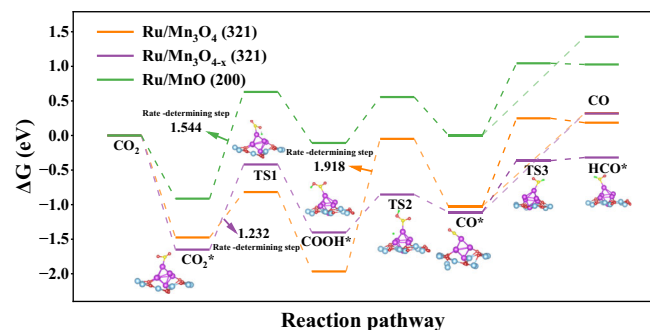


Fig. 4 | Gibbs free energy pathway for the formation of HCO* and CO from CO₂ over Ru/Mn₃O₄ (321), Ru/Mn₃O_{4-x} (321), and Ru/MnO (200). The blue, red, purple, yellow, and green spheres represent the Mn, O, Ru, C, and H atoms, respectively, in the calculation model.

desorption from the catalytic surface as CO is relatively difficult for all the samples⁴⁶. As a result, it is favorable to yield CH₄ via further hydrogenation. It is worth mentioning that in the process of CO₂ hydrogenation, ΔG of RDS over Ru/Mn₃O_{4-x} (1.232 eV) is obviously lower than that on Ru/Mn₃O₄ ($\Delta G = 1.918$ eV) and Ru/MnO ($\Delta G = 1.544$ eV), thus facilitating the subsequent hydrogenation steps toward CH₄. Moreover, as shown in Supplementary Fig. 35, compared with Ru/Mn₃O_{4-x} (321) slabs that simulated dark state, the conduction band that simulated the light state moved to the low energy region, indicating that the involved photons were conducive to electron transfer, which is favorable to CO₂ hydrogenation toward CH₄⁴⁷⁻⁴⁹. Together with the FT-IR spectroscopic characterization above, it was rationalized that the synergy between photon energy and thermal energy favored the formation of COOH*, thus exerting a positive impact on the CO₂ methanation over Ru/MnO_x, which is generated by the partial reduction of Mn₃O₄ by Ru-mediated H-spillover effect in CO₂ hydrogenation⁵⁰.

Based on the spectroscopic and theoretical investigations above, a possible mechanism for photo-thermal-catalytic CO₂ hydrogenation over Ru/MnO_x was proposed. The deposited Ru species is highly efficient for H₂ dissociation. Benefitting from the strong interaction between Ru and MnO_x, Ru-mediated H-spillover effect facilitated the structural evolution of Ru/MnO_x into well-defined Ru/MnO/Mn₃O₄ at low temperature, and the synergy between photon energy and thermal energy could facilitate further hydrogenation of the adsorbed CO₂ molecules over Ru and MnO_x via accelerating the formation of the key intermediate COOH*. Critically, compared to the process of CO evolution from *CO, Ru/Mn₃O_{4-x} is energetically favored for catalyzing *CO hydrogenation toward *HCO, thus promoting the subsequent hydrogenation toward the eventual product of CH₄ with high activity and selectivity.

Discussion

To summarize, a nanostructured Ru/MnO_x photo-thermal catalyst composed of well-defined Ru/MnO/Mn₃O₄ at reaction temperature was assembled for CO₂ hydrogenation toward CH₄. The catalyst illustrated a considerable CO₂ conversion of 66.8% with a superior selectivity of 99.5% and a CH₄ production rate of 166.7 mmol g⁻¹ h⁻¹ at 200 °C. A series of spectroscopic characterizations and theoretical investigations revealed that benefitting from the strong metal-support interaction between Ru and MnO_x, Ru-mediated H-spillover facilitated the structural evolution of Ru/MnO_x into Ru/MnO/Mn₃O₄ at low temperature, and the synergy between photon energy and thermal energy promoted the yield of CH₄ via reducing the activation energy of reaction and facilitating the formation of COOH* species. This work opens up a new way for photo-thermal-enhanced CO₂ hydrogenation toward CH₄.

Methods

Chemicals

MnSO₄·H₂O (99.99%), MnO (99.9%), MnO₂ (99.95%), Mn₂O₃ (99.9%), WO₃ (99.99%) and Ammonium acetate (99.99%) were purchased from Aladdin Chemical Reagent, Ltd. Acetylacetone (99.5%) was provided by Alfa Aesar Chemical Co. Ltd. H₂SO₄ (AR), CH₃COOH (AR) and CH₃OH (99.9%) was purchased from Sinopharm Chemical Reagent Co., Ltd. Ruodium (III) chloride hydrate (99%, Ru 37-40%) and NaOH (96%) were obtained from Beijing InnoChem Science & Technology Co., Ltd. Mn₃O₄ (99.95%) was obtained from Shanghai Macklin Biochemical Technology Co., Ltd. CO₂ (99.995%) and H₂ (99.9995%) were provided by Air Liquid Holding Co., Ltd., China. Deionized water was used in all the experiments.

Materials synthesis

For the synthesis of MnO_x, 1 mmol of MnSO₄·H₂O and 120 mmol of NaOH were dissolved in 30 mL of deionized water with stirring for 0.5 h. The suspension was subsequently transferred into a 100 mL Teflon liner autoclave. The autoclave was heated at 393 K for 12 h, and then cooled to room temperature. The precipitate was washed with distilled water several times until pH = 7, followed by drying in a vacuum at 333 K overnight to obtain the final product.

For the synthesis of Ru/MnO_x, 0.1 g MnO_x, 10 mL of CH₃OH and suitable amount of RuCl₃·3H₂O (0.02, 0.04, 0.06, 0.08, 0.1, 0.12 mmol) were added in 50 mL of deionized water with stirring in a glass reactor (250 mL) with a quartz window. The chamber was evacuated and then filled with Ar of 1 atm and irradiated with 300 W UV-Xe lamp for 1 h in 3 W cm⁻². The precipitate was washed with distilled water several times, followed by drying in a vacuum at 333 K overnight to obtain the final product. Unless otherwise specified, Ru/MnO_x indicates that the added amount of RuCl₃·3H₂O is 0.1 mmol.

Ru/MnO, Ru/Mn₂O₃, Ru/Mn₃O₄, and Ru/MnO₂ were synthesized through an identical procedure. The major difference was that the corresponding commercial support was added to the reaction. 0.1 g MnO, Mn₂O₃, Mn₃O₄ or MnO₂, 10 mL of CH₃OH, and 0.1 mmol RuCl₃·3H₂O were added in 50 mL of deionized water with stirring in a glass reactor (250 mL) with a quartz window. The chamber was evacuated and then filled with Ar of 1 atm and irradiated with 300 W UV-Xe lamp for 1 h in 3 W cm⁻². The precipitate was washed with distilled water several times, followed by drying in a vacuum at 333 K overnight to obtain the final product.

Photo-thermal CO₂ hydrogenation

Photo-thermal CO₂ hydrogenation experiments were carried out in stainless steel reactor of 180 mL (CEL-MPR, Beijing China Education Au-Light Co., Ltd.). In a typical experiment, 15 mg of the catalyst powder was dispersed in 10 mL water in reactor, and the reactor was heated at 333 K overnight to volatilize the solvent and the thin film of catalyst was formed for further experiment (the thickness of the catalyst bed was 25.3 ± 4 μm). Prior to photo-thermal reaction, the reactor was sealed and the air in it was substituted with CO₂ of 1 MPa three times and then CO₂/H₂ mixed gas of 1 MPa with desired ratio was charged at room temperature. Then, the external heating and the 300 W UV-Xe lamp (Beijing China Education Au-Light Co., Ltd) with an intensity of 2.5 W cm⁻² both contributed to maintaining the reactor temperature at 200 °C. After the desired reaction time, the gas products were detected by a gas chromatograph (Agilent GC-8860) and calibrated with a standard gas mixture. To detect liquid products, 10 mL of water was injected into the system after the reaction. Possible liquid products such as methanol, ethanol, acetic acid, and acetaldehyde were detected with an Agilent Technology 7890B gas chromatography system with a flame ionization detector using a DB-WAX-UI column. The possible product formic acid was analyzed by HPLC (Waters 2695) equipped with Aminex HPX-87H column, UV/visible detector (WATER2489), and the mobile phase was 5 mM sulfuric acid

and the flow rate of 0.7 mL/min. The amount of HCHO was analyzed by using the acetylacetone color-development method. Specifically, 1 mL of the as-prepared acetylacetone solution was mixed with 4 mL of the liquid product in a glass bottle, and heated for 5 min in boiling water. The yellow color of the mixed solution was then investigated. Afterwards, a specific amount of solution was taken out, and examined the UV-vis absorption spectrum by using a Shimadzu UV-2700 spectrophotometer. Through the absorbance intensity at 413 nm, the HCHO concentration was obtained. Typically, 100 mL of acetylacetone solution was first prepared by dissolving 15 g of ammonium acetate, 0.3 mL of acetic acid, and 0.2 mL of acetylacetone in water, and was stored in refrigerator with 2–6 °C.

The photothermal CO₂ conversion is also performed in the fixed-bed reactor (CEL-GPPCM, Beijing China Education Au-Light Co., Ltd.) at 200 °C. 150 mg of catalyst and CO₂/H₂ mixed flow (20 mL min⁻¹/80 mL min⁻¹) were used. A 300 W UV-Xe lamp (Beijing China Education Au-Light Co., Ltd) was used as the light source for the reaction (light intensity: 2.5 W cm⁻²). The products in the effluent gas were periodically analyzed by using a gas chromatograph (GC-7920, Beijing China Education Au-Light Co., Ltd.). STY of CH₄ (mol_{CH₄} g⁻¹ h⁻¹), was calculated according to the following equation

$$\text{CH}_4 \text{STY} = \frac{F_{\text{CO}_2, \text{in}} \times X_{\text{CO}_2} \times S_{\text{CH}_4}}{W_{\text{cat}} \times V_m} \quad (1)$$

where F_{CO_2} , it is the volumetric flow rate of CO₂, X_{CO_2} is the CO₂ conversion, S_{CH_4} is the CH₄ selectivity, W_{cat} is the overall mass of catalyst (g), and V_m is the ideal molar volume of CO₂ at standard temperature and pressure.

Materials characterization

The morphology of the samples was characterized by a Zeiss Sigma HD SEM and a JEOL JEM-2100F TEM. The high-angle annular dark-field scanning transmission electron microscope was operated by EM-ARM300F. A Rigaku Ultima VI XRD was employed to record the X-ray diffraction patterns with a scanning speed of 5°/min between 10° and 90°, which was operated at 25 kV and 35 mA with Cu K α radiation. XPS measurements were operated on AXIS Supraelectron spectrometer with Al K α radiation. BET measurements were carried out by N₂ at -196 °C in a Quadrasorb evo. Fourier transform-infrared spectroscopy was performed using Nicolet NEXUS670. UV-VIS-NIR diffuse reflectance spectra were obtained by a UV-VIS-NIR spectrophotometer (UV-3600 Plus, Shimadzu, Japan). Raman analysis was conducted on a Thermo Scientific DXR2 Smart Raman Spectrometer with a 532 nm laser. The adsorption isotherms of CO₂ were determined at 273 K on a BELSORP-max II equipment. A liquid nitrogen-cooled charge-coupled device spectrometer (Princeton Instruments) and a microchannel plate photomultiplier tube (Hamamatsu) combined with time-correlated single photon counting technique (Edinburgh Instruments) were used for photon counting and lifetimes measurements under 375 nm excitation. The Ru contents were quantified by an inductively coupled plasma emission spectrometer (ICP-OES) on an Optima 8300. The H₂-TPR were measured on Micromeritics AutoChem II chemisorption analyzer with a TCD detector, the sample was heated to 200 °C at 10 °C min⁻¹ in an He flow (50 mL min⁻¹) and then cooled to 80 °C. Next, the sample was heated to 700 °C at 20 °C min⁻¹ in a 10% H₂/He mixed flow (50 mL min⁻¹) atmosphere and the outlet gas was detected by TCD. The CO₂-TPD was measured on Micromeritics AutoChem II chemisorption analyzer with a TCD detector. The sample was heated to 200 °C at 10 °C min⁻¹ in an He flow (50 mL min⁻¹) and then cooled to 80 °C. Next, a 10% CO₂/He mixed flow (50 mL min⁻¹) was introduced to the catalyst bed for 0.5 h. The sample was then exposed to He (50 mL min⁻¹) for 0.5 h to remove the weakly adsorbed CO₂ from the surface. Finally, the sample was heated to 700 °C at 10 °C min⁻¹ in a He atmosphere and the outlet gas was detected by TCD. The

temperature of samples was recorded by an infrared thermal imaging camera (Fotric 315, Shanghai Thermal Imaging Technology Co., Ltd.). Considering the limited ability of the reactor window composed of aluminum oxide to penetrate 7–15 μm of infrared light, the image captures the internal temperature of the reactor by quickly removing the reactor window. Variable temperature XRD measurements were collected by an X-ray diffraction patterns (D8 Advance). The samples were heated in CO₂/H₂ mixed flow (10 mL min⁻¹/40 mL min⁻¹) from 25 °C to 200 °C. Data collection after maintaining the specified temperature for 5 min. XPS measurements under variable temperature were operated on Thermo EXCALAB 250Xi electron spectrometer with Al K α radiation. The catalysts were held on the sample holder and activated with illumination in the pretreatment chamber under CO₂/H₂ mixed flow (10 mL min⁻¹/40 mL min⁻¹) from 25 °C to 200 °C. The sample was then introduced into the ultrahigh-vacuum chamber for XPS measurement at room temperature after maintaining the specified temperature for 5 min. FT-IR spectra under variable temperature were recorded with a NICOLET iS50 FTIR spectrometer (Thermo SCIENTIFIC, USA) equipped with a high-temperature reaction chamber and a mercury cadmium telluride (MCT) detector at a resolution of 4 cm⁻¹ and 32 scans per spectrum. The background spectrum was scanned after mixture gas (CO₂:H₂ = 1:4) was introduced. TG-MS analyses were performed on a thermogravimetric analyser (NETZSCH STA449 F3-QMS403D) instrument under air. The catalysts were held on the sample holder and the reactor was sealed until the air in it was substituted with CO₂/H₂ mixed flow (10 mL min⁻¹/40 mL min⁻¹). After that the background spectrum was recorded. Upon reaching the desired temperature through simultaneous external heating and irradiation, the system was maintained for 5 min. Subsequently, the light source was removed for FT-IR measurement. The thickness of the catalyst bed in the batch reactor was measured by laser scanning confocal microscopy LEXT OLS5100.

H-spillover effect detection by WO₃

In a typical experiment, a mixture containing 1 g of WO₃ and 0.015 g of catalyst was placed in a quartz glass culture dish. Then the quartz glass culture dish was placed in stainless steel reactor of 180 mL (CEL-MPR, Beijing China Education Au-Light Co., Ltd.). Prior to photo-thermal reaction, the reactor was sealed, and the air was replaced by H₂ for three times, followed by filling with H₂ (1 MPa). Then, the external heating and the 300 W UV-Xe lamp (Beijing China Education Au-Light Co., Ltd) with an intensity of 0.3 W cm⁻² both contributed to maintain the reactor temperature at 80 °C. After the desired reaction time, the color change of the powder samples was recorded.

The photoelectrochemical (PEC) tests

The photoelectrochemical tests of the samples were carried out on an electrochemical workstation (CHI660e, Chenhua Instrument, Shanghai, China) by using a three-electrode system. The catalyst was drop-coated on clean FTO glass, which was used as a working electrode, while Pt and Ag/AgCl electrodes acted as counter and reference electrodes, respectively. A 300 W Xe lamp (Aulight, Beijing) acted as the light source and all of the electrochemical tests were carried out in 0.1 mol L⁻¹ sodium sulfate solution.

Computational methods

We have employed the Vienna Ab initio Simulation Package to perform all density functional theory (DFT) calculations. The elemental core and valence electrons were represented by the projector augmented wave method and plane-wave basis functions with a cutoff energy of 400 eV. Generalized gradient approximation with the Perdew–Burke–Ernzerh of (GGA-PBE) exchange-correlation functional was employed in all the calculations. Geometry optimizations were performed with the force convergency smaller than 0.05 eV/Å. The spin-polarization effect was also considered. A climbing image nudged

elastic band method was used to locate the transition states with the same convergence standard. The spin-polarization effect was also considered. The DFT-D3 empirical correction method was employed to describe van der Waals interactions. The DFT + U approach was introduced to treat the highly localized Mn 2p states, using parameters of $U-J=4$. For FM of Mn_3O_4 and MnO, the initial magnetic moments of Mn atoms were set to be $+5 \mu\text{B}$. Monkhorst-Pack k-points of $1 \times 1 \times 1$ and $2 \times 2 \times 1$ were applied for all the surface calculations of Ru- Mn_3O_4 and Ru-MnO. Half atoms at bottom were fixed in all the calculation. The Gibbs free energy was calculated by the following equation: $\Delta G = \Delta E + \Delta E_{\text{ZPE}} - T\Delta S$, where the value of ΔE , ΔE_{ZPE} , and ΔS denotes the changes of DFT energy, the zero-point energy and the entropy at 473.15 K, respectively.

Data availability

The data supporting the findings of this work are available within the article and its Supplementary Information files. All the data reported in this work are available from the authors. Source data are provided with this paper.

References

1. He, M., Sun, Y. & Han, B. Green carbon science: scientific basis for integrating carbon resource processing, utilization, and recycling. *Angew. Chem. Int. Ed.* **52**, 9620–9633 (2013).
2. Gao, P., Zhong, L., Han, B., He, M. & Sun, Y. Green carbon science: keeping the pace in practice. *Angew. Chem. Int. Ed.* **61**, e202210095 (2022).
3. He, M., Sun, Y. & Han, B. Green carbon science: efficient carbon resource processing, utilization, and recycling towards carbon neutrality. *Angew. Chem. Int. Ed.* **61**, e202112835 (2022).
4. Zhao, T., Yang, Z., Tang, Y., Liu, J. & Wang, F. Advances and perspectives of photopromoted CO_2 hydrogenation for methane production: catalyst development and mechanism investigations. *Energy Fuels* **36**, 6711–6735 (2022).
5. Zhou, B., Li, J., Dong, X. & Yao, L. GaN nanowires/Si photocathodes for CO_2 reduction towards solar fuels and chemicals: advances, challenges, and prospects. *Science China. Chemistry* **66**, 739–754 (2023).
6. Len, T. & Luque, R. Addressing the CO_2 challenge through thermocatalytic hydrogenation to carbon monoxide, methanol and methane. *Green. Chem.* **25**, 490–521 (2023).
7. Li, Y. et al. Recent advances in photothermal CO_x conversion. *Sol. RRL* **6**, 2200493 (2022).
8. Hong, J. et al. Photothermal chemistry based on solar energy: from synergistic effects to practical applications. *Adv. Sci.* **9**, 2103926 (2022).
9. Ghossoub, M., Xia, M., Duchesne, P. N., Segal, D. & Ozin, G. Principles of photothermal gas-phase heterogeneous CO_2 catalysis. *Energy Environ. Sci.* **12**, 1122–1142 (2019).
10. Liu, H. et al. Recent progress on photothermal heterogeneous catalysts for CO_2 conversion reactions. *Energy Technol.* **10**, 2100804 (2022).
11. Zhou B., Sun S. Approaching the commercial threshold of solar water splitting toward hydrogen by III-nitrides nanowires. *Front. Energy*, <https://doi.org/10.1007/s11708-023-0870-z> (2023).
12. Lv, C. et al. Nanostructured materials for photothermal carbon dioxide hydrogenation: regulating solar utilization and catalytic performance. *ACS Nano* **17**, 1725–1738 (2023).
13. Jiang, H. et al. Light-driven CO_2 methanation over Au-grafted $\text{Ce}_{0.95}\text{Ru}_{0.05}\text{O}_2$ solid-solution catalysts with activities approaching the thermodynamic limit. *Nat. Catal.* **6**, 519–530 (2023).
14. He, Z. et al. Photothermal CO_2 hydrogenation to hydrocarbons over trimetallic Co–Cu–Mn catalysts. *Green. Chem.* **23**, 5775–5785 (2021).
15. Chen, Y. et al. Cooperative catalysis coupling photo-/photothermal effect to drive Sabatier reaction with unprecedented conversion and selectivity. *Joule* **5**, 3235–3251 (2021).
16. Marques Mota, F. & Kim, D. H. From CO_2 methanation to ambitious long-chain hydrocarbons: alternative fuels paving the path to sustainability. *Chem. Rev.* **48**, 205–259 (2019).
17. Yan, Q.-Q. et al. Reversing the charge transfer between platinum and sulfur-doped carbon support for electrocatalytic hydrogen evolution. *Nat. Commun.* **10**, 4977 (2019).
18. Dong, T. et al. Ru decorated TiO_x nanoparticles via laser bombardment for photothermal co-catalytic CO_2 hydrogenation to methane with high selectivity. *Appl. Catal. B: Environ.* **326**, 122176 (2023).
19. Yin, C., Chen, J., Pan, C.-L., Pan, Y. & Hu, J. MOF-derived Mn_3O_4 @C hierarchical nanospheres as cathodes for aqueous Zinc-Ion batteries. *ACS Appl. Energy Mater.* **5**, 14144–14154 (2022).
20. Dreyer, J. A. H. et al. Influence of the oxide support reducibility on the CO_2 methanation over Ru-based catalysts. *Appl. Catal. B Environ.* **219**, 715–726 (2017).
21. Liu, P. et al. Photochemical route for synthesizing atomically dispersed palladium catalysts. *Science* **352**, 797–800 (2016).
22. Chen, R., Yu, J. & Xiao, W. Hierarchically porous MnO_2 microspheres with enhanced adsorption performance. *J. Mater. Chem. A* **1**, 11682–11690 (2013).
23. Stebounova, L. V., Gonzalez-Pech, N. I., Peters, T. M. & Grassian, V. H. Physicochemical properties of air discharge-generated manganese oxide nanoparticles: comparison to welding fumes. *Environ. Sci. Nano* **5**, 696–707 (2018).
24. Hao, X.-L., Zhao, J.-Z. & Zhao, Y. Aqueous synthesis of Mn_3O_4 nanoparticle@ MnOOH nanobelt heterostructures. *J. Nanosci. Nanotechnol.* **18**, 4318–4323 (2018).
25. Ristić, M. et al. Synthesis and long-term phase stability of Mn_3O_4 nanoparticles. *J. Mol. Struct.* **1044**, 255–261 (2013).
26. Li, N. et al. Enhanced norfloxacin degradation by visible-light-driven $\text{Mn}_3\text{O}_4/\gamma\text{-MnOOH}$ photocatalysis under a weak magnetic field. *Sci. Total Environ.* **761**, 143268 (2021).
27. Zhang, J. et al. Porous carbon encapsulated Mn_3O_4 for stable lithium storage and its ex-situ XPS study. *Electrochim. Acta* **319**, 518–526 (2019).
28. Wang, X., Lan, G., Liu, H., Zhu, Y. & Li, Y. Effect of acidity and ruthenium species on catalytic performance of ruthenium catalysts for acetylene hydrochlorination. *Catal. Sci. Technol.* **8**, 6143–6149 (2018).
29. Zhang, J. et al. Constructing epitaxially grown heterointerface of metal nanoparticles and manganese dioxide anode for high-capacity and high-rate lithium-ion batteries. *Nanoscale* **13**, 20119–20125 (2021).
30. Song, C., Wang, Z., Yin, Z., Xiao, D. & Ma, D. Principles and applications of photothermal catalysis. *Chem. Catal.* **2**, 52–83 (2022).
31. Zhang, F. et al. Photothermal catalytic CO_2 reduction over nanomaterials. *Chem. Catal.* **1**, 272–297 (2021).
32. Zhai, J. et al. Photocatalytic cleavage of $\text{C}(\text{sp}^3)\text{-N}$ bond in trialkylamines to dialkylamines and olefins. *ChemSusChem* **15**, e202201119 (2022).
33. Zhai, J. et al. Selective photocatalytic aerobic oxidation of methane into carbon monoxide over $\text{Ag}/\text{AgCl}/\text{SiO}_2$. *Chem. Sci.* **13**, 4616–4622 (2022).
34. Zheng, J. & Lei, Z. Incorporation of CoO nanoparticles in 3D marigold flower-like hierarchical architecture MnCo_2O_4 for highly boosting solar light photo-oxidation and reduction ability. *Appl. Catal. B Environ.* **237**, 1–8 (2018).
35. Fu, R. et al. Defect ZrO_{2-x} supported Ru nanoparticles as Mott-Schottky photocatalyst for efficient ammonia synthesis at ambient conditions. *Green Chem.* **25**, 8531 (2023).

36. Guo, Y. et al. Low-temperature CO₂ methanation over CeO₂-supported Ru single atoms, nanoclusters, and nanoparticles competitively tuned by strong metal–support interactions and H-Spillover effect. *ACS Catal.* **8**, 6203–6215 (2018).
37. Liu, X. et al. Strong interaction over Ru/defects-rich aluminium oxide boosts photothermal CO₂ methanation via microchannel flow-type system. *Adv. Energy Mater.* **12**, 2201009 (2022).
38. Bose, V. C. & Biju, V. Mixed valence nanostructured Mn₃O₄ for supercapacitor applications. *Bull. Mater. Sci.* **38**, 865–873 (2015).
39. Wang, C. et al. Product selectivity controlled by nanoporous environments in zeolite crystals enveloping rhodium nanoparticle catalysts for CO₂ hydrogenation. *J. Am. Chem. Soc.* **141**, 8482–8488 (2019).
40. Xing, S. et al. Improving the efficiency of hydrogen spillover by an organic molecular decoration strategy for enhanced catalytic hydrogenation performance. *ACS Catal.* **13**, 4003–4011 (2023).
41. Jia, X., Zhang, X., Rui, N., Hu, X. & Liu, C.-j Structural effect of Ni/ZrO₂ catalyst on CO₂ methanation with enhanced activity. *Appl. Catal. B Environ.* **244**, 159–169 (2019).
42. Mo, Q. et al. Unexpected insulating polymer maneuvered solar CO₂-to-syngas conversion. *Adv. Funct. Mater.* **33**, 2210332 (2022).
43. Li, C., Domen, K., Maruya, K.-i & Onishi, T. Spectroscopic identification of adsorbed species derived from adsorption and decomposition of formic acid, methanol, and formaldehyde on cerium oxide. *J. Catal.* **125**, 445–455 (1990).
44. Zhang, T. et al. The dual-active-site tandem catalyst containing Ru single atoms and Ni nanoparticles boosts CO₂ methanation. *Appl. Catal. B Environ.* **323**, 122190 (2023).
45. Yang, M., Yuan, H., Wang, H. & Hu, P. Insights into the selective catalytic reduction of NO by NH₃ over Mn₃O₄(110): a DFT study coupled with microkinetic analysis. *Sci. China Chem.* **61**, 457–467 (2018).
46. Sun, Q.-M. et al. Boosted inner surface charge transfer in perovskite nanodots@mesoporous titania frameworks for efficient and selective photocatalytic CO₂ reduction to methane. *Angew. Chem. Int. Ed.* **61**, e202200872 (2022).
47. Li, Y. et al. Experimental and theoretical insights into an enhanced CO₂ methanation mechanism over a Ru-based catalyst. *Appl. Catal. B Environ.* **319**, 121903 (2022).
48. Li, Y. et al. Robust photo-assisted removal of NO at room temperature: experimental and density functional theory calculation with optical carrier. *Green Energy Environ.* **8**, 1102–1116 (2023).
49. Yang, X. et al. Oxygen vacancy-induced spin polarization of tungsten oxide nanowires for efficient photocatalytic reduction and immobilization of uranium(VI) under simulated solar light. *Appl. Catal. B Environ.* **324**, 122202 (2023).
50. Xin, H. et al. Overturning CO₂ hydrogenation selectivity with high activity via reaction-induced strong metal–support interactions. *J. Am. Chem. Soc.* **144**, 4874–4882 (2022).

Acknowledgements

The work was supported by the National Key Research and Development Program of China (2023YFA1507901, 2020YFA0710201)

(H.H.W.), the National Natural Science Foundation of China (22109095 (B.W.Z.), 21890761 (B.X.H.), 22121002 (B.X.H.)), the Research Funds of Happiness Flower ECNU (2020ST2203) (B.X.H.), Shanghai Pilot Program for Basic Research-Shanghai Jiao Tong University (No. 21TQ1400211) (B.W.Z.).

Author contributions

J.X.Z., B.W.Z., H.H.W., M.Y.H., and B.X.H. proposed the project, designed the experiments, and wrote the manuscript; J.X.Z. performed the whole experiments; Z.H.X., X.T., X.C., J.P.J., S.Q.J., B.W.Z., H.H.W., M.Y.H., and B.X.H. assisted in analyzing the experimental data; B.W.Z., H.H.W., M.Y.H., and B.X.H. co-supervised the whole project. All authors discussed the results and commented on the manuscript. All the authors contributed to the overall scientific interpretation and wrote the manuscript.

Competing interests

The authors declare no competing interests.

Additional information

Supplementary information The online version contains supplementary material available at <https://doi.org/10.1038/s41467-024-45389-7>.

Correspondence and requests for materials should be addressed to Baowen Zhou, Haihong Wu, Mingyuan He or Buxing Han.

Peer review information *Nature Communications* thanks Juan Coronado, Dequan Xiao, and Diego Mateo for their contribution to the peer review of this work. A peer review file is available.

Reprints and permissions information is available at <http://www.nature.com/reprints>

Publisher's note Springer Nature remains neutral with regard to jurisdictional claims in published maps and institutional affiliations.

Open Access This article is licensed under a Creative Commons Attribution 4.0 International License, which permits use, sharing, adaptation, distribution and reproduction in any medium or format, as long as you give appropriate credit to the original author(s) and the source, provide a link to the Creative Commons licence, and indicate if changes were made. The images or other third party material in this article are included in the article's Creative Commons licence, unless indicated otherwise in a credit line to the material. If material is not included in the article's Creative Commons licence and your intended use is not permitted by statutory regulation or exceeds the permitted use, you will need to obtain permission directly from the copyright holder. To view a copy of this licence, visit <http://creativecommons.org/licenses/by/4.0/>.

© The Author(s) 2024